AIAA JOURNAL
Vol. 49, No. 5, May 2011

Application of a Discontinuous Galerkin Method to Discretize Acoustic Perturbation Equations

Marcus Bauer,* Jürgen Dierke,* and Roland Ewert*
DLR, German Aerospace Center, 38108 Braunschweig, Germany

DOI: 10.2514/1.J050333

Airframe noise of complex geometries, such as high-lift airfoil configurations, may conveniently be computed on unstructured grids. A discontinuous Galerkin method provides a robust high-order-accurate discretization of systems of partial differential equations like, for example, the acoustic perturbation equations, even on this type of grid. In particular, a discontinuous Galerkin method based on Lagrange polynomials may be used, since it enables simple and cheap truncation of flux terms. The goal of the work reported herein is to verify such a discontinuous Galerkin method. Therefore, the sound field of a monopole situated in a laminar boundary layer is computed. Computations are stable, free from spurious numerical oscillations, and show very good agreement with other computations and with theoretical results.

I. Introduction

AIRFRAME noise is generated through the transformation of turbulent energy into acoustic energy in the vicinity of edges, such as the trailing or side edge of an airfoil profile. It significantly contributes to the overall noise level of modern airliners, especially during the approach and landing phases of flight, when the engines are throttled back. Then, the main sources of airframe noise are the landing gear and the high-lift system with its deployed slats and flaps, which are geometrically complex objects.

Broadband airframe noise as an important contribution to airframe noise can efficiently be computed with a hybrid computational fluid dynamics (CFD)/computational aeroacoustics (CAA) approach [1–3]; see Fig. 1. First, a CFD code computes the time-averaged flow around the object under consideration as a solution of the Reynolds-averaged Navier–Stokes (RANS) equations. Second, a CAA code computes the unsteady generation and propagation of sound by solving the acoustic perturbation equations (APE) [1,4,5], a variant of the linearized Euler equations (LEE). Their unknowns depend both on space and time, whereas their coefficients are merely space dependent, and are thus given by the preceding RANS computation. In contrast to the LEE, the APE exclude the nonacoustic modes of vorticity and entropy. Thus, they follow to be stable for arbitrary mean flowfields, i.e., no instability waves as in the LEE can occur [1,4,5]. Furthermore, the source term of the APE fully controls the perturbation vorticity in the solution, and no vorticity exists beyond the source regions. On the other hand, the wave operator encoded in the left-hand side of the APE is exact only in case of an irrotational mean flowfield, whereas mean vorticity causes errors in the computed sound propagation. However, these errors are assumed to be small for mild levels of mean vorticity [4,5]. The unsteady turbulent source term on the right-hand side of the APE may efficiently be computed with the fast random particle mesh (FRPM) method [3,6], which stochastically synthesizes a turbulent velocity field from RANS data. Dealing with complex objects, unstructured computational grids are strongly preferred to block-structured ones. Then, the discontinuous Galerkin method (DGM) may be used to discretize systems of partial differential equations (PDEs) like the APE, since it provides a robust, efficient high-order-accurate discretization, even on unstructured grids.

In particular, discontinuous Galerkin (DG) formulations based on Lagrange polynomials have become more and more popular in the field of CAA [3,7–11], because the nodes associated to this family of shape functions provide some favorable properties. In such DG formulations, all field quantities are spatially represented by Lagrange polynomials of a certain degree p inside the individual elements. The specialty is, that even products of field quantities are represented by the same Lagrange polynomials; that is, they are quite vigorously truncated to polynomial degree p. If, for instance, two quantities represented by polynomials of degree p are multiplied with each other, the product actually is a polynomial of degree $2p$. This kind of truncation is very easy and efficient through the Lagrangian nodes and will be called Lagrange truncation in the present work.

Considering the APE, it is the flux quantities, being products of unknown perturbation variables and time-averaged mean flow quantities, which are subject to Langrange truncation from polynomial degree $2p$ to degree p. The truncation is effective in areas of nonuniform mean flow, like in boundary layers. Inherently, it does not occur in uniform mean flow. Nonuniform mean flow causes refraction of sound, which is a prominent aeroacoustic phenomenon. Thus, the performance of Lagrange truncation applied to the APE in the framework of a DGM should be checked thoroughly.

Rasetarinera et al. [7,8] computed the acoustic response of various objects to an incoming, periodic, vortical gust in two space dimensions. They solved the full nonlinear Euler equations employing a DGM based on Lagrange truncation. The method was found to be stable, even without additional artificial damping, and results are in good agreement with other solutions.

Ehrenfried et al. [9] proposed the use of Lagrange truncation to compute the sound field of a model monopole sound source situated in a simplified laminar boundary layer. The governing equations were given by a system of first-order PDEs derived from Möhring's acoustic analogy. Thus, the unknowns were the perturbations of the stagnation enthalpy and of the mass flux, the latter being the product of density and velocity. Computations were performed on a two-dimensional (2-D) triangular mesh. They were stable, and results were free from spurious numerical oscillations. The maximum of the acoustic directivity occurred close to the theoretical critical angle [12,13]. Furthermore, even the so-called channeled waves were well resolved. These are sound waves, which are refracted toward the wall by the mean flow just to be reflected off the wall to be refracted toward the wall again. Thus, they are captured in the boundary layer and are subject to permanent refraction. As expected for the employed nonviscous setting, their amplitude remained constant in

Presented as Paper 2009-3175 at the 15th AIAA/CEAS Aeroacoustics Conference, Miami, FL, 11–13 May 2009; received 5 November 2009; revision received 3 December 2010; accepted for publication 19 December 2010.

*Research Engineer, Institute of Aerodynamics and Flow Technology, Technical Acoustics, Lilienthalplatz 7. Member AIAA.

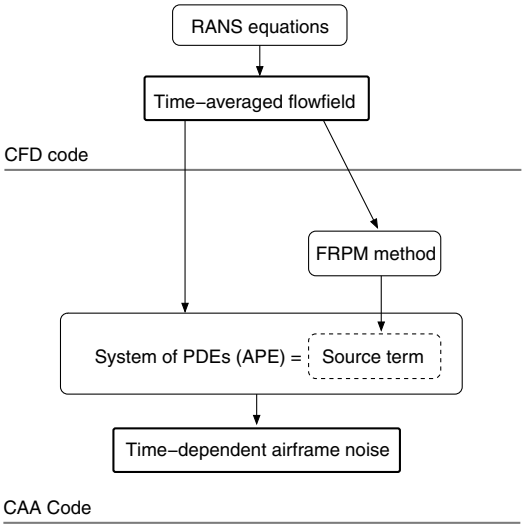

Fig. 1 Hybrid CFD/CAA approach for efficient prediction of broadband airframe noise.

the downstream boundary layer. In addition, their wavelength matched that from a modal analysis.

Rao and Morris [10,11] used Lagrange truncation to solve the LEE. They combined it with the simple Lax–Friedrich formula to approximate the unique upwind-biased edge normal flux along the interelement boundaries. That way, propagation of sound waves through a shear layer was computed in two dimensions. Unfortunately, solutions contained spurious oscillations, which were found to be sensitive to the dissipation parameter α of the Lax–Friedrich flux. Such difficulties are not reported in [7–9], even though Lagrange truncation was used. The explanation probably is that more elaborate flux formulas were employed in those works, namely, the characteristics-based flux formula in [9] and Roe's approximate Riemann solver [14] in [7,8]. This assumption is supported by a detailed study of spatially propagating waves using a DG scheme [15]. A system of one-dimensional (1-D) linear, hyperbolic equations was considered, and spurious oscillations were found to occur with the simple Lax–Friedrich flux formula and not with the exact characteristics-based flux formula.

In the current work, a DGM based on Lagrange truncation is used to provide the spatial discretization of the APE in two dimensions on a triangular mesh. Both the unknown perturbation quantities and the time-averaged mean flow quantities are approximated by Lagrange polynomials of degree $p = 3$ in each element. Lagrange truncation is applied to the flux quantities. Time integration is performed by the fourth-order-accurate explicit standard Runge–Kutta scheme as a first step.

The goal of the present work is verify the particular DGM when applied to discretize the APE. Therefore, the test case of a monopole in a boundary layer [9,12,13] is reconsidered. In contrast with [9], the unknowns of the APE are the descriptive perturbations of pressure and velocity and not the slightly unorthodox perturbations of stagnation enthalpy and mass flux. Thus, APE results can be more easily compared with other simulations and with theory than results from [9].

Section II of this paper describes the employed DG-APE method: the APE are briefly outlined, followed by a detailed description of the DG method. Results computed for the test case of a monopole in a boundary layer are presented in Sec. III, and conclusions are drawn in Sec. IV.

II. Method

A. Acoustic Perturbation Equations

Four different formulations of the APE were proposed [4]. The most popular APE-4 system, which is also considered here, reads in symbolic notation

$$\frac{\partial p'}{\partial t} + c_0^2 \nabla \cdot \left(\varrho_0 \boldsymbol{u}' + \boldsymbol{u}_0 \frac{p'}{c_0^2} \right) = c_0^2 q_c$$

$$\frac{\partial \boldsymbol{u}'}{\partial t} + \nabla(\boldsymbol{u}_0 \cdot \boldsymbol{u}') + \nabla\left(\frac{p'}{\varrho_0} \right) = \boldsymbol{q}_m \tag{1}$$

In Eqs. (1), t denotes time, p denotes pressure, ϱ denotes density, and $\boldsymbol{u}$ denotes the velocity vector. A prime marks unknown time- and space-dependent perturbation variables, whereas subscript 0 identifies time-averaged given mean flow quantities. The speed of sound is named c_0. The right-hand-side symbols q_c and $\boldsymbol{q}_m$ denote the sources. The exact sources follow by rewriting the homogeneous Navier–Stokes equations in primitive nonlinear disturbance form, so that the left-hand side equals that from Eqs. (1) [4]. For vortex sound problems like airframe noise, all viscous, nonlinear, and entropy-related source contributions may be neglected [1,4], resulting in $q_c = 0$ and $\boldsymbol{q}_m = -\boldsymbol{L}'$, where $\boldsymbol{L}\prime$ is the linear perturbed Lamb vector, $\boldsymbol{L}' = \boldsymbol{\omega}' \times \boldsymbol{u}_0 + \boldsymbol{\omega}_0 \times \boldsymbol{u}'$, expressed in terms of the vorticity vector $\boldsymbol{\omega} = \nabla \times \boldsymbol{u}$. Actually, no external sources are employed in this work; that is, q_c and $\boldsymbol{q}_m$ are both zero. However, they are kept for the sake of generality.

Using 2-D Cartesian coordinates and assuming constant sound speed c_0, a reasonable assumption for airframe noise problems, the APE from Eqs. (1), read in matrix vector notation

$$\frac{\partial \boldsymbol{U}}{\partial t} + \frac{\partial \boldsymbol{F}^x}{\partial x} + \frac{\partial \boldsymbol{F}^y}{\partial y} - \boldsymbol{S} = 0 \tag{2}$$

where x and y denote the spatial coordinates, and $\boldsymbol{U}$ and $\boldsymbol{S}$ stand for

$$\boldsymbol{U} = \begin{pmatrix} p' \\ u' \\ v' \end{pmatrix}, \qquad \boldsymbol{S} = \begin{pmatrix} c_0^2 q_c \\ q_m^x \\ q_m^y \end{pmatrix} \tag{3}$$

Accordingly, the velocity vector and the source vector associated to the momentum equations are given by $\boldsymbol{u} = [u, v]^T$ and $\boldsymbol{q}_m = [q_m^x, q_m^y]^T$, respectively. The symbols $\boldsymbol{F}^x$ and $\boldsymbol{F}^y$,

$$\boldsymbol{F}^x = \boldsymbol{A}\boldsymbol{U}, \qquad \boldsymbol{F}^y = \boldsymbol{B}\boldsymbol{U} \tag{4}$$

are denoted as flux vectors in this work. Matrices $\boldsymbol{A}$ and $\boldsymbol{B}$ contain the mean flow quantities

$$\boldsymbol{A} = \begin{pmatrix} u_0 & \varrho_0 c_0^2 & 0 \\ \frac{1}{\varrho_0} & u_0 & v_0 \\ 0 & 0 & 0 \end{pmatrix}, \qquad \boldsymbol{B} = \begin{pmatrix} v_0 & 0 & \varrho_0 c_0^2 \\ 0 & 0 & 0 \\ \frac{1}{\varrho_0} & u_0 & v_0 \end{pmatrix} \tag{5}$$

The fluxes are nothing but the aforementioned products of mean flow and perturbation quantities, which will be subject to Lagrange truncation in the framework of the upcoming DG discretization.

B. Discretization of Acoustic Perturbation Equations via the Discontinuous Galerkin Method

1. *Approximate Representation of Field Variables*

The 2-D computational domain is partitioned into nonoverlapping triangular elements $E^{(m)}$, with superscript (m) denoting the element number, where the field variables are represented by an expansion of type

$$f^{(m)} \approx \tilde{f}^{(m)} = \sum_{l=1}^{N} \hat{f}_l^{(m)}(t) \cdot \Phi_l^{(m)}(x, y) \tag{6}$$

The number N of expansion terms depends on the polynomial degree p of the expansion. According to the Pascal triangle [16], the relationship is

$$N = \frac{(p+1)(p+2)}{2} \tag{7}$$

in 2-D. In this work, $p = 3$ is used, yielding $N = 10$. The symbols $\hat{f}_l^{(m)}$ denote the expansion coefficients, whereas $\Phi_l^{(m)}$ are spatial shape functions given by Lagrange polynomials; see [16]. Lagrange

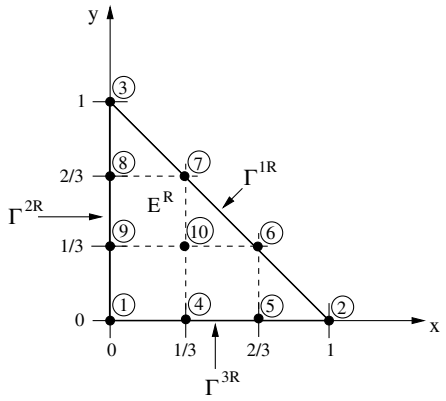

Fig. 2 Right-angled reference triangle E^R with nodes 1 to 10 of employed shape functions of degree three; nodes 1 to 3 coincide with triangle vertices, and edges Γ^{jR} are numbered after their facing vertex.

polynomials give every expansion coefficient $\hat{f}_l^{(m)}$ the descriptive meaning of the value of the approximation $\tilde{f}^{(m)}$ at one certain position $\vec{\boldsymbol{x}}_l^{(m)}$ in element $E^{(m)}$. These positions are the so-called nodes. Accordingly, the value of shape function $\Phi_k^{(m)}$ at node $\vec{\boldsymbol{x}}_l^{(m)}$ is

$$\Phi_k^{(m)}(\vec{\boldsymbol{x}}_l^{(m)}) = \begin{cases} 1, & l = k \\ 0, & l \neq k \end{cases} \tag{8}$$

The physical element shape functions $\Phi_k^{(m)}(x, y)$ will be deduced through coordinate transform from reference shape functions $\Phi_k^R(x, y)$ defined on the reference triangle E^R. Figure 2 shows the reference triangle E^R as well as the distribution of the nodes on E^R, and Fig. 3 illustrates some of the corresponding reference shape functions $\Phi_k^R(x, y)$.

All the variables from the APE are expanded in the fashion of Eq. (6). This includes the quantities p', u', v', ϱ_0, $\frac{1}{\varrho_0}$, u_0, and v_0, as well as the components F_r^x, F_r^y, and S_r, $r \in \{1, 2, 3\}$, of the flux vectors and of the source vector, respectively. Thus, the source just has to be known at the Lagrangian nodes $\vec{\boldsymbol{x}}_l^{(m)}$ to readily determine the DG source coefficients $\hat{S}_{rl}^{(m)}$.[†] The coefficients associated with mean flow quantities are not time dependent and are, for example, given through a RANS solution. The actual unknowns are the unsteady coefficients $\hat{p}_l'^{(m)}(t)$, $\hat{u}_l'^{(m)}(t)$, and $\hat{v}_l'^{(m)}(t)$.

No continuity of the overall approximate solution is enforced at element interfaces in the framework of the DGM. Consequently, p', u', and v' become discontinuous along interelement boundaries. Usually, however, the discontinuities are very small.

The approximate flux quantities $\tilde{F}_r^x$ and $\tilde{F}_r^y$ are products of mean and perturbation quantities; thus, they are actually polynomials of degree $2p$. But, in order to save computational effort, they are truncated to degree p, and they are pproximated in the fashion of Eq. (6). The truncation is especially simple through the Lagrangian nodes. The product $\tilde{F}_r^{x(m)} = \tilde{A}_{rq}^{(m)} \tilde{U}_q^{(m)}$ is, for example, approximated as

$$\tilde{F}_r^{x(m)} = \hat{F}_{rl}^{x(m)} \Phi_l^{(m)} \quad \text{with} \quad \hat{F}_{rl}^{x(m)} = (\hat{A}_{rq}^{(m)} \hat{U}_q^{(m)})_l \tag{9}$$

regarding the summation convention for repeated subscripts. As $l \in \{1, \ldots, N\}$, N matrices $\hat{\boldsymbol{A}}^{(m)}$ have to be provided in each element $E^{(m)}$, so that the lth of these matrices, which consists of the mean flow quantities at node $\vec{\boldsymbol{x}}_l^{(m)}$ (i.e., $\hat{\boldsymbol{A}}_l^{(m)}$), is multiplied with column l of matrix $\hat{\boldsymbol{U}}^{(m)} = [\hat{U}_{ql}^{(m)}]$ to construct the lth column of matrix $\hat{\boldsymbol{F}}^{x(m)} = [\hat{F}_{rl}^{x(m)}]$. Analogously, $\tilde{F}_r^{y(m)} = \tilde{B}_{rq}^{(m)} \tilde{U}_q^{(m)}$ is computed as

$$\tilde{F}_r^{y(m)} = \hat{F}_{rl}^{y(m)} \Phi_l^{(m)} \quad \text{with} \quad \hat{F}_{rl}^{y(m)} = (\hat{B}_{rq}^{(m)} \hat{U}_q^{(m)})_l \tag{10}$$

[†]Symbols with double subscripts, such as $\hat{S}_{rl}^{(m)}$, may be seen as matrix entries, where the first subscript indicates its row and the second its column in the matrix.

In other words, the product of two polynomials of degree p is approximated as follows. One set of Lagrange polynomials of degree p with a certain distribution of nodes is chosen to represent both polynomials to be multiplied. Then, simply, corresponding nodal values are multiplied, and the same Lagrange polynomials of degree p still represent the course of the product between the new nodal values, which actually has a polynomial degree of $2p$. However, the truncated product is exact at the nodes.

Atkins and Lockard [17,18] and Atkins and Shu [19,20] propose an expansion of the fluxes to a polynomial degree of at least $p + 1$ in order to maintain the design rate of convergence of $p + 1$. The convergence rate was found to drop to approximately p when truncating the flux at polynomial degree p in 1-D tests with the nonlinear Burgers equation [19,20]. Atkins and Lockard [17,18] and Atkins and Shu [19,20] employed monomials as shape functions. If their observations also hold for the proposed DGM based on Lagrange polynomials, then an order of four would actually only prevail in a uniform mean flowfield, whereas it may drop to three in domains of nonuniform mean flow. However, this is not considered a problem. No stability or accuracy problems were encountered with the proposed DGM; see the results from [7–9] and the results presented in the current work.

2. *Elementwise Integration of Weighted Residuals*

Next, Eq. (2) is considered in index notation, index $r \in \{1, 2, 3\}$, and elementwise approximations $\tilde{U}_r^{(m)}$, $\tilde{F}_r^{x(m)}$, $\tilde{F}_r^{y(m)}$, and $\tilde{S}_r^{(m)}$ are substituted for the respective exact distributions. Thus, each of the PDEs encoded in system (2) yields a time- and space-dependent residual, which is the smaller, the better the approximate solution. To obtain a high quality approximate solution, and as the next step toward the DG discretization of the APE, elementwise integrals of the spatially weighted residuals are set equal to zero. The residuals are weighted with the shape functions $\Phi_k^{(m)}$ themselves, $k \in \{1, \ldots, N\}$, a procedure known as Galerkin weighting. Subsequent integration by parts finally leads to the weak form of the APE according to Eq. (2):

$$\underbrace{\int_{E^{(m)}} \Phi_k^{(m)} \frac{\partial \tilde{U}_r^{(m)}}{\partial t} \, \mathrm{d}\Omega}_{I1} + \sum_{j=1}^{3} \underbrace{\int_{\Gamma^{j(m)}} \Phi_k^{(m)} \tilde{F}_r^n \, \mathrm{d}\Gamma}_{I2j} - \underbrace{\int_{E^{(m)}} \frac{\partial \Phi_k^{(m)}}{\partial x} \tilde{F}_r^{x(m)} \, \mathrm{d}\Omega}_{I3}$$
$$- \underbrace{\int_{E^{(m)}} \frac{\partial \Phi_k^{(m)}}{\partial y} \tilde{F}_r^{y(m)} \, \mathrm{d}\Omega}_{I4} - \underbrace{\int_{E^{(m)}} \Phi_k^{(m)} \tilde{S}_r^{(m)} \, \mathrm{d}\Omega}_{I5} = 0 \tag{11}$$

Considering the line integrals $I2j$, $\Gamma^{j(m)}$ denotes the jth edge of triangle $E^{(m)}$, and $\boldsymbol{n}^{j(m)}$ is the outward pointing unit normal vector of that edge. Consequently,

$$\tilde{F}_r^n = \tilde{F}_r^x n_x^{j(m)} + \tilde{F}_r^y n_y^{j(m)} \tag{12}$$

is component r of the approximate edge normal flux related to edge $\Gamma^{j(m)}$. Thus, $\tilde{F}_r^n$ actually is shorthand for $\tilde{F}_r^{nj(m)}$. Considering Eqs. (4), $\tilde{F}_r^n$ from Eq. (12) becomes

$$\tilde{F}_r^n = \tilde{C}_{rq}^{j(m)} \tilde{U}_q \tag{13}$$

with

$$\tilde{C}_{rq}^{j(m)} = n_x^{j(m)} \tilde{A}_{rq}^{(m)} + n_y^{j(m)} \tilde{B}_{rq}^{(m)} \tag{14}$$

There is no element superscript for $\tilde{U}_q$ in Eq. (13), because the approximate solutions from adjacent elements are, in general, discontinuous along the inner edges of the computational domain. This issue (i.e., the calculation of the line integrals $I2j$) is the subject of Sec. II.B.4.

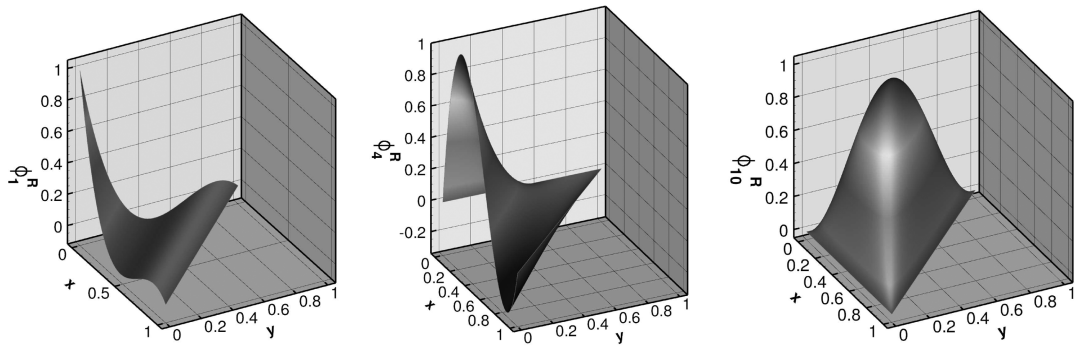

Fig. 3 Reference shape functions Φ_1^R, Φ_4^R, and Φ_{10}^R given in terms of Lagrange polynomials of degree three.

3. Surface Integrals

The calculation of the surface integrals $I1$, $I3$, $I4$, and $I5$ from Eq. (11) is illustrated by way of integral $I3$. Replacing $\tilde{F}_r^{x(m)}$ in terms of expansion equation (6) leads to

$$I3 = \int_{E^{(m)}} \frac{\partial \Phi_k^{(m)}}{\partial x} \hat{F}_{rl}^{x(m)} \Phi_l^{(m)} \, \mathrm{d}\Omega \tag{15}$$

The physical shape functions $\Phi_k^{(m)}(x, y)$ are expressed through the reference shape functions $\Phi_k^R(x, y)$ like

$$\Phi_k^{(m)}(x, y) = \Phi_k^R[\xi^{(m)}(x, y), \eta^{(m)}(x, y)] \tag{16}$$

where $\xi^{(m)}$ and $\eta^{(m)}$ are coordinates local to element $E^{(m)}$. The Appendix describes the relationship between coordinates x, y and coordinates $\xi^{(m)}, \eta^{(m)}$. For simplicity, the coordinate transform is linear [19,20]. Inserting Eq. (16) into Eq. (15) (i.e., substituting coordinates $\xi^{(m)}, \eta^{(m)}$ for coordinates x, y) and applying the chain rule results in

$$I3 = \hat{F}_{rl}^{x(m)} \int_0^1 \int_0^{1-\xi^{(m)}} \left[\frac{\partial \Phi_k^R(\xi^{(m)}, \eta^{(m)})}{\partial \xi^{(m)}} \frac{\partial \xi^{(m)}}{\partial x} + \frac{\partial \Phi_k^R(\xi^{(m)}, \eta^{(m)})}{\partial \eta^{(m)}} \frac{\partial \eta^{(m)}}{\partial x} \right] \cdot \Phi_l^R(\xi^{(m)}, \eta^{(m)}) J^{(m)} \, \mathrm{d}\eta^{(m)} \, \mathrm{d}\xi^{(m)} \tag{17}$$

where $J^{(m)}$ is the Jacobian, Eq. (A3), which is constant for each triangle $E^{(m)}$ due to the simple linear coordinate transform and is just twice its area. The derivatives $\partial \xi^{(m)}/\partial x$ and $\partial \eta^{(m)}/\partial x$ are obtained from Eqs. (A2). Renaming the integration variables x and y finally yields

$$I3 = (y_3^{(m)} - y_1^{(m)}) \hat{F}_{rl}^{x(m)} \underbrace{\int_0^1 \int_0^{1-x} \frac{\partial \Phi_k^R(x, y)}{\partial x} \Phi_l^R(x, y) \, \mathrm{d}y \, \mathrm{d}x}_{K_{lk}^x} + (y_1^{(m)} - y_2^{(m)}) \hat{F}_{rl}^{x(m)} \underbrace{\int_0^1 \int_0^{1-x} \frac{\partial \Phi_k^R(x, y)}{\partial y} \Phi_l^R(x, y) \, \mathrm{d}y \, \mathrm{d}x}_{K_{lk}^y} \tag{18}$$

where, for example, $y_1^{(m)}$ denotes the y coordinate of vertex 1 of triangle $E^{(m)}$. The remaining surface integrals are calculated analogously. Altogether, they become

$$I1 = J^{(m)} \frac{\partial \hat{U}_{rl}^{(m)}}{\partial t} M_{lk} \tag{19}$$

$$I3 = (y_3^{(m)} - y_1^{(m)}) \hat{F}_{rl}^{x(m)} K_{lk}^x + (y_1^{(m)} - y_2^{(m)}) \hat{F}_{rl}^{x(m)} K_{lk}^y \tag{20}$$

$$I4 = (x_1^{(m)} - x_3^{(m)}) \hat{F}_{rl}^{y(m)} K_{lk}^x + (x_2^{(m)} - x_1^{(m)}) \hat{F}_{rl}^{y(m)} K_{lk}^y \tag{21}$$

$$I5 = J^{(m)} \hat{S}_{rl}^{(m)} M_{lk} \tag{22}$$

where the entries of the so-called mass matrix $\boldsymbol{M}$ and of the so-called stiffness matrices $\boldsymbol{K}^x$ and $\boldsymbol{K}^y$ are obtained as integrals over the reference triangle

$$M_{lk} = \int_0^1 \int_0^{1-x} \Phi_k^R(x, y) \Phi_l^R(x, y) \, \mathrm{d}y \, \mathrm{d}x \tag{23}$$

$$K_{lk}^x = \int_0^1 \int_0^{1-x} \frac{\partial \Phi_k^R(x, y)}{\partial x} \Phi_l^R(x, y) \, \mathrm{d}y \, \mathrm{d}x \tag{24}$$

$$K_{lk}^y = \int_0^1 \int_0^{1-x} \frac{\partial \Phi_k^R(x, y)}{\partial y} \Phi_l^R(x, y) \, \mathrm{d}y \, \mathrm{d}x \tag{25}$$

4. Line Integrals

To solve the line integrals $I2j$ from Eq. (11), a parameter χ, $0 \le \chi \le 1$, is introduced to scan triangle edge $\Gamma^{j(m)}$

$$I2j = \int_0^1 \Phi_k^{(m)}[x(\chi, j, m), y(\chi, j, m)] \tilde{F}_r^n(\chi, t) \times \sqrt{\left[\frac{\partial x(\chi, j, m)}{\partial \chi}\right]^2 + \left[\frac{\partial y(\chi, j, m)}{\partial \chi}\right]^2} \, \mathrm{d}\chi \tag{26}$$

The points $(x, y) = [x(\chi, j, m), y(\chi, j, m)]$ lie along edge $\Gamma^{j(m)}$. The edges are supposed to be scanned anticlockwise as χ increases. Actually, however, no functions $x(\chi, j, m)$ and $y(\chi, j, m)$ are required, as the values of $\Phi_k^{(m)}$ along the physical edges can be deduced from the values of the reference shape functions Φ_k^R along the edges of the reference triangle like

$$\Phi_k^{(m)}[x(\chi, j, m), y(\chi, j, m)] = \Phi_k^R[\alpha(\chi, j), \beta(\chi, j)] \tag{27}$$

where the coordinates $(x, y) = [\alpha(\chi, j), \beta(\chi, j)]$ lie along edge Γ^{jR} of reference triangle E^R; recall Fig. 2:

$$\begin{aligned} [\alpha(\chi, 1), \beta(\chi, 1)] &= (1 - \chi, \chi) \\ [\alpha(\chi, 2), \beta(\chi, 2)] &= (0, 1 - \chi) \\ [\alpha(\chi, 3), \beta(\chi, 3)] &= (\chi, 0) \end{aligned} \tag{28}$$

No substitution of the integration variable χ from Eq. (26) occurs through the application of Eq. (27). Furthermore, the square-root expression from Eq. (26) simply represents length $L^{j(m)}$ of edge $\Gamma^{j(m)}$, so that one obtains

$$I2j = L^{j(m)} \int_0^1 \Phi_k^R[\alpha(\chi, j), \beta(\chi, j)] \tilde{F}_r^n(\chi, t) \, \mathrm{d}\chi \tag{29}$$

Next, an approximate polynomial expansion is substituted for $\tilde{F}_r^n(\chi, t)$. In opposition to the surface integrals, no 2-D expansion of type equation (6) but a simpler 1-D expansion is employed. However, like the 2-D expansion, it is also based on Lagrange polynomials of degree p and reads

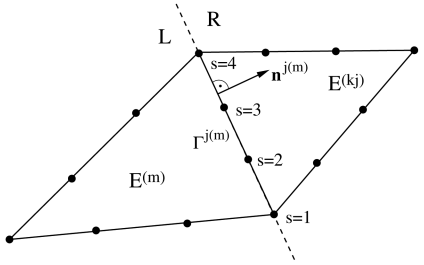

Fig. 4 Illustration of 1-D Riemann problem along an inner edge $\Gamma^{j(m)}$; element $E^{(kj)}$ denotes the element $E^{(m)}$ neighbor along edge $\Gamma^{j(m)}$.

$$\tilde{F}^{\,n}_{\,r}(\chi,t)=\sum_{s=1}^{N^{1D}}\hat{F}^{n}_{rs}(t)\cdot\Phi^{1D}_{s}(\chi) \tag{30}$$

where the number of expansion terms is $N^{1D}=p+1$. One-dimensional Lagrange polynomials of degree $p=3$, with nodes at $\chi=0,\frac{1}{3},\frac{2}{3}$, and 1 were chosen as spatial shape functions $\Phi^{1D}_{s}(\chi)$ (see [16]), and the nodes s are arranged anticlockwise along the edges.

The line integrals $I2j$ finally become

$$I2j=L^{j(m)}\hat{F}^{n}_{rs}G^{j}_{sk} \tag{31}$$

with

$$G^{j}_{sk}=\int_{0}^{1}\Phi^{R}_{k}[\alpha(\chi,j),\beta(\chi,j)]\Phi^{1D}_{s}(\chi)\,\mathrm{d}\chi \tag{32}$$

What remains is the calculation of the edge normal flux coefficients $\hat{F}^{n}_{rs}$.

As mentioned in Sec. II.B.2, the edge normal flux is indefinite along the inner edges. Therefore, the coefficients $\hat{F}^{n}_{rs}$ for a node s along edge $\Gamma^{j(m)}$ are calculated as follows: the 1-D Riemann initial value problem for the APE in the edge normal direction is considered for this node. The mean flow at the node is assumed to span the entire space. The discontinuous perturbation quantities from the two adjacent elements are assumed to span the complete domains L and R separated by the (extended) edge $\Gamma^{j(m)}$ hosting the node. Figure 4 illustrates the situation. Within the scope of these assumptions, the coefficients $\hat{F}^{n}_{rs}$ can be obtained exactly through the characteristics-based flux formula:

$$\hat{F}^{\,n}_{\,rs}=\hat{F}^{nj(m)}_{rs}=\{\tfrac{1}{2}[\hat{C}^{(m)}_{rq}+|\hat{C}^{(m)}_{rq}|]\hat{U}^{(m)}_{q}+\tfrac{1}{2}[\hat{C}^{(m)}_{rq}-|\hat{C}^{(m)}_{rq}|]\hat{U}^{(kj)}_{q}\}_{s} \tag{33}$$

where $E^{(kj)}$ is the element $E^{(m)}$ neighbor along edge $\Gamma^{j(m)}$. Furthermore,

$$\hat{U}^{\,(m)}_{\,qs}=\hat{U}^{(m)}_{ql^{+}(s,j)} \tag{34}$$

$$\hat{U}^{\,(kj)}_{\,qs}=\hat{U}^{(kj)}_{ql^{-}(s,i)} \tag{35}$$

where the functions $l^{+}(s,j)$ and $l^{-}(s,i)$ assign element node $l\in\{1,\ldots,N\}$ to edge node $s\in\{1,\ldots,N^{1D}\}$. Symbol i denotes the local edge number of $\Gamma^{j(m)}$ in the neighboring triangle $E^{(kj)}$. Table 1 lists the values of $l^{+}(s,j)$. As the triangle vertices are numbered anticlockwise by the employed CENTAUR grid generator[‡] in each triangle, l^{-} results from l^{+} by swapping the column order of Table 1. Figure 5 illustrates the situation. The matrices $\hat{\boldsymbol{C}}^{(m)}_{s}$ from Eq. (33) are calculated according to Eq. (14) as

Table 1 Values of function $l^{+}(s,j)$, i.e., element node l corresponding to node s from edge j when edges are scanned anticlockwise

	$s=1$	$s=2$	$s=3$	$s=4$
$j=1$	2	6	7	3
$j=2$	3	8	9	1
$j=3$	1	4	5	2

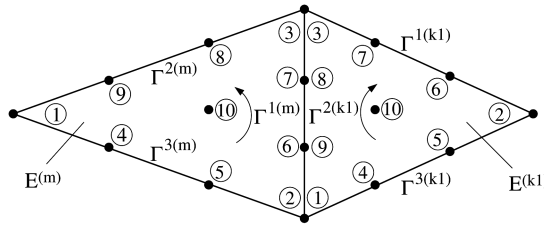

Fig. 5 Exemplary proximity relationship between an element $E^{(m)}$ and its neighbor $E^{(k1)}$.

$$\hat{\boldsymbol{C}}^{\,(m)}_{\,s}=n^{j(m)}_{x}\hat{\boldsymbol{A}}^{(m)}_{l^{+}(s,j)}+n^{j(m)}_{y}\hat{\boldsymbol{B}}^{(m)}_{l^{+}(s,j)} \tag{36}$$

Since the mean flow coefficients at an edge node are not discontinuous, they may be taken from either of the two elements adjacent to edge $\Gamma^{j(m)}$. Element $E^{(m)}$ is picked here. The matrices $|\hat{\boldsymbol{C}}^{(m)}_{s}|$ are given by

$$|\hat{\boldsymbol{C}}^{(m)}_{s}|=\boldsymbol{R}\,|\boldsymbol{D}|\,\boldsymbol{R}^{-1} \tag{37}$$

with matrix $\boldsymbol{R}$ consisting of the eigenvectors of $\hat{\boldsymbol{C}}^{(m)}_{s}$ and the diagonal matrix $\boldsymbol{D}$ made up of its eigenvalues. To simplify matters, Eq. (33) is actually evaluated with the help of a transformation into local edge-aligned coordinates (not elaborated on here for the sake of brevity).

If edge $\Gamma^{j(m)}$ lies along a solid wall boundary of the computational domain, then there is no neighbor $E^{(kj)}$ to element $E^{(m)}$. Consequently, the approximate solution is not discontinuous, and Eq. (13) can be written as

$$\tilde{F}^{\,n}_{\,r}=\tilde{C}^{j(m)}_{rq}\tilde{U}^{(m)}_{q} \tag{38}$$

Thus, the edge normal flux coefficients for edge node s are

$$\hat{F}^{\,n}_{\,rs}=(\hat{C}^{j(m)}_{rq}\hat{U}^{(m)}_{q})_{s} \tag{39}$$

Next, $u_0=v_0=0$ and $n^{j(m)}_{x}u'+n^{j(m)}_{y}v'=0$ are applied to Eq. (39), so that the wall boundary condition is realized by

$$\hat{F}^{\,n}_{\,rs}=(\hat{W}^{j(m)}_{rq}\hat{U}^{(m)}_{q})_{s} \tag{40}$$

with wall matrices $\hat{\boldsymbol{W}}^{j(m)}_{s}$ given in terms of function $l^{+}(s,j)$ (Table 1) by

$$\hat{\boldsymbol{W}}^{\,j(m)}_{\,s}=\begin{pmatrix}0 & 0 & 0\\ n^{j(m)}_{x}/\hat{\varrho}^{(m)}_{0l^{+}(s,j)} & 0 & 0\\ n^{j(m)}_{y}/\hat{\varrho}^{(m)}_{0l^{+}(s,j)} & 0 & 0\end{pmatrix} \tag{41}$$

and $\hat{U}^{(m)}_{qs}$ obeying Eq. (34).

A far-field boundary condition is meant to pretend that the related triangle edges are inner edges of the computational domain. However, the solution along inner edges is inherently discontinuous in the framework of the DGM. Thus, Eqs. (38) and (39), which assume no occurrence of discontinuities, do not yield a reasonable far-field boundary condition as one could think. Instead, a far-field boundary condition is realized by simply ignoring the contribution from missing element $E^{(kj)}$ in Eq. (33) as a first step [9,21]:

$$\hat{F}^{\,n}_{\,rs}=\{\tfrac{1}{2}[\hat{C}^{(m)}_{rq}+|\hat{C}^{(m)}_{rq}|]\hat{U}^{(m)}_{q}\}_{s} \tag{42}$$

This boundary allows sound waves, for which the wave fronts are aligned with the edge, to exit without reflection, whereas part of the

[‡]Data available at http://www.centaursoft.com [retrieved 16 February 2011].

waves is reflected otherwise. More elaborate DG far-field boundary conditions are, for example, proposed in [21,22].

5. Semidiscrete Discontinuous Galerkin Formulation

Inserting Eqs. (19–22), as well as Eq. (31), into Eq. (11) and rearranging the difference of integrals I3 and I4 yields

$$J^{(m)}\frac{\partial \hat{U}_{rl}^{(m)}}{\partial t}M_{lk}+\sum_{j=1}^{3}L^{j(m)}\hat{F}_{rs}^{n}G_{sk}^{j}-[(y_3^{(m)}-y_1^{(m)})\hat{F}_{rl}^{x(m)} + (x_1^{(m)}-x_3^{(m)})\hat{F}_{rl}^{y(m)}]K_{lk}^{x}-[(y_1^{(m)}-y_2^{(m)})\hat{F}_{rl}^{x(m)} + (x_2^{(m)}-x_1^{(m)})\hat{F}_{rl}^{y(m)}]K_{lk}^{y}-J^{(m)}\hat{S}_{rl}^{(m)}M_{lk}=0 \tag{43}$$

Substituting flux coefficients $\hat{F}_{rl}^{x(m)}$ and $\hat{F}_{rl}^{y(m)}$ according to Eqs. (9) and (10), respectively, introducing matrices

$$\hat{\boldsymbol{X}}_l^{(m)}=(y_3^{(m)}-y_1^{(m)})\hat{\boldsymbol{A}}_l^{(m)}+(x_1^{(m)}-x_3^{(m)})\hat{\boldsymbol{B}}_l^{(m)}$$
$$\hat{\boldsymbol{Y}}_l^{(m)}=(y_1^{(m)}-y_2^{(m)})\hat{\boldsymbol{A}}_l^{(m)}+(x_2^{(m)}-x_1^{(m)})\hat{\boldsymbol{B}}_l^{(m)} \tag{44}$$

and solving for $\partial \hat{U}_{rl}^{(m)}/\partial t$, gives

$$\frac{\partial \hat{U}_{rl}^{(m)}}{\partial t}=\frac{1}{J^{(m)}}\left[(\hat{X}_{rq}\hat{U}_q)_l^{(m)}K_{lk}^{x}M_{kl}^{-1}+(\hat{Y}_{rq}\hat{U}_q)_l^{(m)}K_{lk}^{y}M_{kl}^{-1} - \sum_{j=1}^{3}L^{j(m)}\hat{F}_{rs}^{n}G_{sk}^{j}M_{kl}^{-1}\right]+\hat{S}_{rl}^{(m)} \tag{45}$$

The coefficients $\hat{F}_{rs}^{n}$ are calculated via Eq. (33), Eq. (40), or Eq. (42) according to the type of edge $\Gamma^{j(m)}$ (inner edge, wall boundary edge, or far-field boundary edge, respectively).

6. Time Integration

Time integration is performed by the common standard explicit fourth-order-accurate Runge–Kutta (RK4) scheme based on the values of $\partial \hat{\boldsymbol{U}}^{(m)}/\partial t$ from Eq. (45). As spatial shape functions of degree three are used, the overall order of accuracy of the method is four, which was verified by convergence tests. The Courant–Friedrichs–Lewy (CFL) number used to satisfy the stability condition for the RK4 scheme is [23]

$$\mathrm{CFL}=\frac{1}{2p+1}=0.1429 \tag{46}$$

First, element time-step sizes $dt^{(m)}$ are estimated in terms of this CFL number like

$$dt^{(m)}=\mathrm{CFL}\frac{h_{\min}^{(m)}}{c_0+\sqrt{(\hat{u}_{010}^{(m)})^2+(\hat{v}_{010}^{(m)})^2}} \tag{47}$$

from the mean flow values at each center node $l=10$ using the minimum height $h_{\min}^{(m)}$ of each triangular element. The finally employed global time step is then

$$dt=f_s\cdot\min(dt^{(m)}) \tag{48}$$

where f_s is a safety factor of 0.8 or 0.9.

7. Practical Realization

The proposed DG discretization of the APE was implemented in the programming language FORTRAN 90/95. Except for $\hat{U}_{ql}^{(m)}$, $\hat{S}_{rl}^{(m)}$, and $\hat{F}_{rs}^{n}$, all quantities from Eq. (45) are time independent and are computed and stored before time integration. The matrices $\boldsymbol{M}$, $\boldsymbol{K}^x$, $\boldsymbol{K}^y$, and $\boldsymbol{G}^j$, according to Eqs. (23–25) and (32), respectively, are calculated exactly using 1-D and 2-D Gaussian-type quadrature formulas [16,24]. The inverse mass matrix $\boldsymbol{M}^{-1}$ is obtained via Gauss–Jordan elimination [25]. Matrix products $\boldsymbol{K}^x\boldsymbol{M}^{-1}$, $\boldsymbol{K}^y\boldsymbol{M}^{-1}$, and $\boldsymbol{G}^j\boldsymbol{M}^{-1}$ are computed before time integration. To save memory and computational effort during time integration, the flux formula equation (33) is only evaluated once for nodes along inner edges. When the coefficients $\hat{F}_{rs}^{n}=\hat{F}_{rs}^{nj(m)}$ have been calculated, then the coefficients from the angle of the neighboring triangle $E^{(kj)}$ are readily given by $\hat{F}_{rs}^{ni(kj)}=-\hat{F}_{r\sigma}^{nj(m)}$ with $\sigma=N_{1D}+1-s$, $s\in\{1,\ldots,N_{1D}\}$. Again, i is the local edge number of $\Gamma^{j(m)}$ in neighbor $E^{(kj)}$.

III. Sound Field of Monopole in Boundary Layer

A. Test Setup

The mean flowfield was given by a simplified laminar boundary of constant thickness; see next. Dimensionless quantities were used. They relate to dimensional quantities marked by superscript $*$ or subscript ∞, like

$$t=t^*\frac{c_\infty}{\delta^*},\qquad \boldsymbol{x}=\frac{\boldsymbol{x}^*}{\delta^*},\qquad \varrho=\frac{\varrho^*}{\varrho_\infty}$$
$$\boldsymbol{u}=\frac{\boldsymbol{u}^*}{c_\infty},\qquad p=\frac{p^*}{\varrho_\infty c_\infty^2} \tag{49}$$

where $\boldsymbol{x}=[x,y]^T$ is the coordinate vector. The dimensional reference quantities are the constant boundary-layer thickness δ^* as well as the density ϱ_∞ and the speed of sound c_∞, both at infinity.

Figure 6 illustrates the test setup. The plane wall ran along $y=0$, and the monopole model was located in the coordinate origin. Polar coordinates r and θ were used for data postprocessing.

The boundary-layer velocity profile was defined by a polynomial of degree four [9], and the freestream Mach number was $Ma_\infty=0.3$. Explicitly, the dimensionless mean flow variables were given by $\varrho_0=1$,

$$u_0=\begin{cases}Ma_\infty(2y-2y^3+y^4), & 0\le y\le 1\\ Ma_\infty, & y>1\end{cases} \tag{50}$$

$v_0=0$. This simplified laminar boundary layer neglects the fact that the thickness actually increases when freestream velocity and density (and temperature) are constant. Nevertheless, it is considered appropriate to investigate the ability of the proposed DGM to handle a nonuniform mean flowfield.

The monopole model may be deemed a plane sound wave of amplitude one and wavelength $\lambda=1$, which traveled into positive y direction and entered the computational domain through the wall triangle edge of length $\epsilon=0.1$, centered at the coordinate origin [9]; see Fig. 7 (right). It was realized by computing the flux coefficients along this very edge according to Eq. (33), like for an inner edge, and the solution coefficients from an imaginary neighbor $E^{(kj)}$ situated below the x axis were given by $\hat{\boldsymbol{U}}_s^{(kj)}=[\sin(2\pi t),0,\sin(2\pi t)]^T$. The flux coefficients associated to the other edges along $y=0$ were computed according to the usual solid wall boundary condition [Eq. (40)]. It had been shown that the sound field produced by such a monopole model is indeed nearly nondirectional, i.e., independent of angle θ in a quiescent medium $u_0=v_0=0$ [9].

Comparative computations were performed with DLR, German Aerospace Center's (DLR's) well-established CAA code PIANO [26], which employs the widespread fourth-order-accurate dispersion relation preserving [27] finite difference scheme for the spatial discretization of the APE. For time integration, the standard fourth-

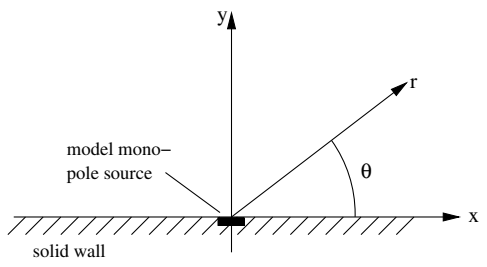

Fig. 6 Coordinates used for simulations with monopole in boundary layer.

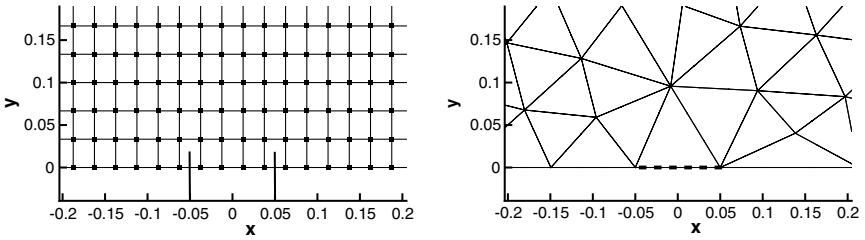

Fig. 7 Close-ups of computational grids in region of monopole sound source: coarse block-structured grid for PIANO (left) and medium-fine DG grid (right).

order explicit Runge–Kutta scheme, which is also used in the DG-APE code, was chosen. The elaborate radiation boundary condition by Tam and Webb [27] was applied to far-field boundaries, whereas solid walls were treated with the ghost point concept of Tam and Dong [28]. Artificial selective damping attenuated spurious short waves [29]. The preceding monopole model was realized in terms of the nonreflective characteristics boundary condition of Thompson [30].

Three different unstructured triangular grids were used for the DG computations and two different structured grids for the PIANO simulations. All were refined upstream of the source to ensure a certain minimum resolution per wavelength.

The coarse DG grid consisted of $I = 8772$ elements with a ratio of triangle edge length to acoustic wavelength of $\frac{L}{\lambda} \leq \frac{1}{2}$. The medium and fine DG grids are characterized by $I = 18,136$ ($\frac{L}{\lambda} \leq \frac{1}{3}$) and $I = 31,301$ ($\frac{L}{\lambda} \leq \frac{1}{4}$), respectively. All DG grids were additionally refined in the vicinity of the source, so that the length of the source edge was $\epsilon = 0.1$ in each grid. As becomes apparent next, the domain covered by the DG grids was semicircular. This was due to the simple nonreflective far-field boundary condition [Eq. (40)], which was used as a first step.

Both structured PIANO grids consisted of one single rectangular block covering the domain $-16 \leq x \leq 31$ and $0 \leq y \leq 16$. They were also refined in the vicinity of the source. Four grid points were used between $-0.05 \leq x \leq 0.05$ to prescribe the incoming plane wave with the Thompson boundary condition [Fig. 7 (left)]. The grid spacing was kept constant in the vicinity of the source to obtain a stable solution. The coarser grid had a minimum resolution of about eight points per wavelength (PPW) and consisted of $470 \times 210 = 98,700$ grid points, whereas the finer grid offered at least 12 PPW using $640 \times 310 = 198,400$ grid points.

B. Results

1. *Contour Plots*

Figure 8 is a snapshot of the p' distribution computed with the DG-APE method on the medium-fine grid. The mean velocity profile causes clockwise refraction of sound in the boundary layer, so that a shadow zone develops upstream of the source and channeled waves can be observed along the downstream wall [12,13]. All DG-APE computations were stable and free from spurious numerical oscillations.

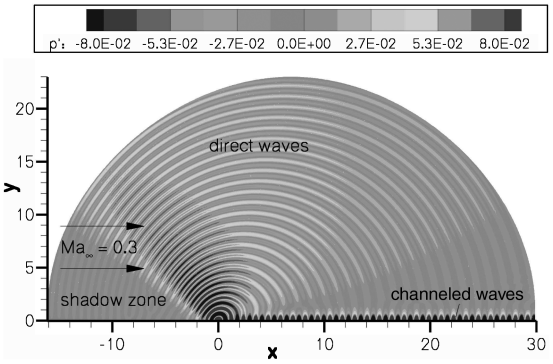

Fig. 8 Pressure perturbation field of monopole sound source in boundary layer computed with DG-APE code on medium-fine grid.

Figure 9 shows p' contour plots from APE solutions obtained with the DGM and with PIANO. To think a little outside the box, a contour plot from a direct numerical simulation (DNS) performed by Suzuki and Lele [12,13] is also included. Comparing DG and PIANO, there is excellent agreement of the sound radiation pattern, indicating the employed DGM based on Lagrange truncation works very well. The absolute contour levels differ due to a higher amplitude of the monopole model in DG. Here, focus is actually on sound propagation, however, and these different contour levels are not significant. Contour plots from the various PIANO or DG grids are practically identical, except the solution on the coarsest DG grid, where the amplitude of the sound waves decays a little faster (not shown). Agreement with the DNS is good. Minor differences occur, e.g., in the shadow zone upstream of the source. There, the amplitude of the so-called diffracted waves is slightly higher in the APE computations than in the DNS. As shown next, the main reason for the slight deviations is the fact that the wave operator encoded in the left-hand side of the APE is exact only for an irrotational mean flowfield, whereas the DNS does not make assumptions on sound propagation. Some other potential reasons for deviations could be as follows:

1) The monopole was not modeled by a plane wave entering the computational domain through an imaginary hole in the wall in the DNS. Instead, a periodically oscillating Gaussian-shaped source

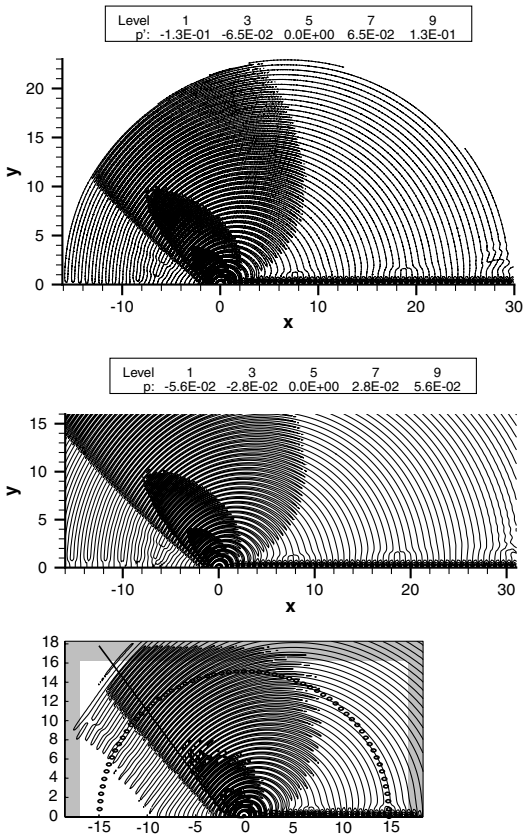

Fig. 9 Pressure perturbation field of monopole sound source in boundary layer as computed with DG-APE code on medium-fine grid (top), with PIANO on coarse grid (center), and with DNS [12] (bottom).

distribution centered at $(x, y) = (0, 0.019)$ was employed. However, since the wavelength of the sound waves is around unity, they hardly see the little distance of $\Delta y = 0.019$ from the wall, so these two monopole models are regarded nearly identical.

2) A boundary-layer profile based on the compressible Blasius boundary-layer equation was used in the DNS. Accordingly, in contrast to the simplified boundary layer used for DG and PIANO, density, temperature, and boundary-layer thickness were not constant. The spreading rate of the boundary layer was less than 0.1% in the DNS, however.

3) Furthermore, the sound field seems to be a little underresolved in the DNS; see Fig. 9. The underlying grid consisted of $560 \times 400 = 224,000$ points, and high-order Padé finite difference schemes provided the spatial discretization of the Navier–Stokes equations [12,13].

2. *Directivities*

Directivities $\Gamma(\theta)$ were calculated from the pressure root-mean square $\tilde{p}$ along path $r = 15, 0° \leq \theta \leq 180°$. The underlying pressure signal $p'(t)$ was monitored at 500 equally distributed points on this path in the DG computations, resulting in $\Delta\theta_{\mathrm{DG}} = 0.36°$. The value of a field variable can readily be computed at arbitrary locations by evaluation of Eq. (6) in the framework of the DG method. Two hundred and fifty points close to the path were picked as observer locations in the PIANO grids, resulting in $\Delta\theta_{\mathrm{PIANO}} \approx 0.72°$. The actual θ coordinates of the observation points were taken into account in the processing of the PIANO data, whereas the tiny deviations from $r = 15$ were neglected. Sixty adequate points were selected in the DNS, so that $\Delta\theta_{\mathrm{DNS}} \approx 3°$. Position errors were corrected in data postprocessing [12,13].

First of all, Fig. 10 compares directivities $\Gamma(\theta) = \tilde{p}(\theta)$ from the three DG grids. The main maximum is always encountered at $\theta = 0°$; that is, it is caused by the channeled waves. The solution from the coarse grid is somewhat rough, and its amplitude is a little too low. The solution on the medium-fine grid is much smoother and practically identical to that on the fine grid. Thus, a ratio of triangle edge length to resolvable acoustic wavelength of $\frac{L}{\lambda} \leq \frac{1}{3}$ is recommended for highly accurate results. However, grids of ratio $\frac{L}{\lambda} \leq \frac{1}{2}$, as realized in the coarse DG grid, have turned out to be sufficiently fine for practical purposes [3].

Figure 11 compares directivities $\Gamma(\theta) = \tilde{p}(\theta)/\tilde{p}_{\mathrm{ref}}$ from DG and PIANO. The reference value $\tilde{p}_{\mathrm{ref}}$ was the individual maximum of $\tilde{p}$ in the region of the direct waves in each case. Excellent agreement can be stated, even for low values of θ, i.e., for the channeled waves. As mentioned before, the truncation of the fluxes to polynomial degree p in the framework of the DGM is effective in areas of a spatially varying mean flowfield, i.e., in the boundary layer. Since the channeled waves are captured right in the boundary layer, where they are subject to permanent refraction, they are well suited to check the truncation of the fluxes. The excellent agreement of the directivities, even at low angles, proves the truncation works very well and clearly verifies the employed DGM based on Lagrange truncation. Tiny differences are probably only due to the different number of virtual microphones along the directivity path. As mentioned previously, $\Delta\theta_{\mathrm{DG}} = 0.36°$, whereas $\Delta\theta_{\mathrm{PIANO}} \approx 0.72°$. However, data points are simply connected by straight lines in the directivity plots. The directivity from the coarse PIANO grid is practically identical to that from the fine PIANO grid shown in Fig. 11.

To think a little outside the box again, Fig. 12 compares normalized directivities from three simulations: PIANO-APE, PIANO-LEE, and DNS. Next to the APE, DLR's PIANO code can also solve the LEE. Recall from the Fig. 11 that the PIANO-APE solution is practically identical to the DG-APE result.

According to the left graph of Fig. 12, the direct sound field from the three computations matches quite well. As a slight difference, the APE predict the peak angle at $\theta \approx 126°$, whereas it appears at $\theta \approx 129°$ in the other two solutions. The right graph of Fig. 12 shows that the amplitude of the channeled waves is nearly identical in the

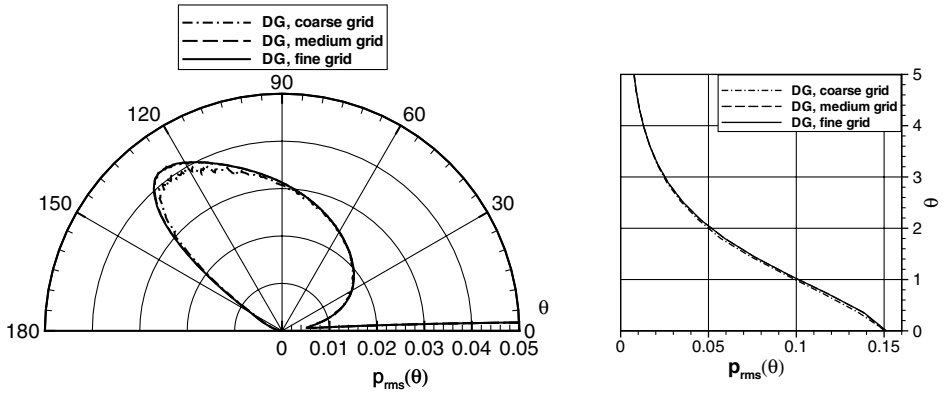

Fig. 10 Unscaled directivities $\Gamma(\theta) = \tilde{p}(\theta)$ of monopole in boundary layer obtained on three DG grids; the right graph is a close-up of the channeled wave region.

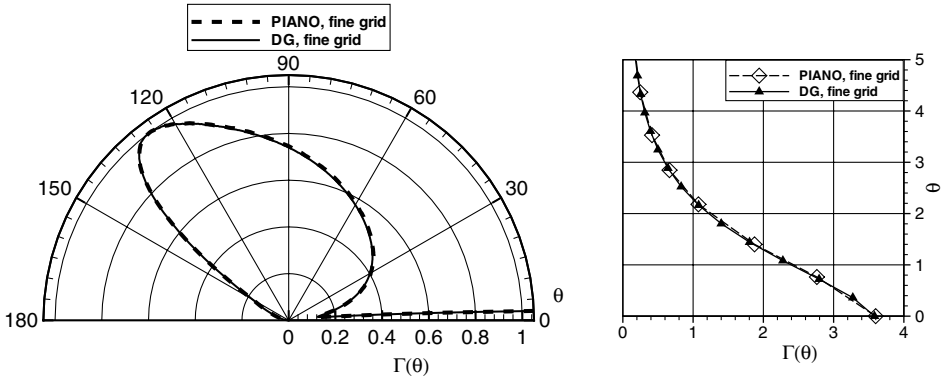

Fig. 11 Directivities $\Gamma(\theta) = \tilde{p}(\theta)/\tilde{p}_{\mathrm{ref}}$ of monopole in boundary layer obtained with DG and PIANO; the reference value $\tilde{p}_{\mathrm{ref}}$ is the maximum of $\tilde{p}$ in the region of direct waves for each curve, and the right graph is a close-up of the channeled wave region.

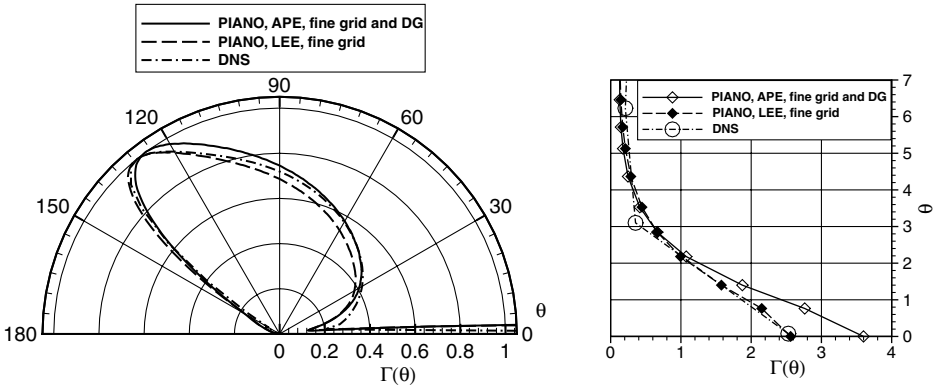

Fig. 12 Directivities $\Gamma(\theta) = \tilde{p}(\theta)/\tilde{p}_{\mathrm{ref}}$ of monopole in boundary layer from PIANO using APE and LEE and from DNS; the reference value $\tilde{p}_{\mathrm{ref}}$ is the maximum of $\tilde{p}$ in the region of direct waves for each curve, and the right graph is a close-up of the channeled wave region.

solutions from DNS and LEE, whereas it is somewhat higher in the APE solution. Considering these observations, the APE obviously slightly overpredict the refraction of sound in the boundary layer.

The fact that the LEE solution agrees better with the DNS than the APE result confirms the preceding argument, from the discussion of Fig. 9, that most of the slight deviations between APE and DNS are due to the APE simplified wave operator being exact for an irrotational mean flowfield. To assess the APE-related error from nonzero mean vorticity ω_0, a Strouhal number based on ω_0 and on sound frequency f was introduced as $St = f/|\omega_0|$ in [5]. The absolute value of the mean vorticity may be assessed like $|\omega_0| \approx \Delta u_0/\delta$ here, where δ is the constant boundary-layer thickness [5]. Substituting $f = 1$, $\Delta u_0 = Ma_\infty = 0.3$, and $\delta = 1$ gives $St \approx 3.\overline{33}$; that is, the Strouhal number is of order $\mathcal{O}(1)$ here. Since this is considerably below the irrotational limit $St \to \infty$, the error induced by the APE is regarded acceptable.

As already indicated in the introduction, the APE have some crucial advantages over the LEE, especially when predicting airframe noise in the framework of a hybrid approach, as sketched in Fig. 1. These are caused by the fact that the APE exclude the nonacoustic mode of vorticity. (The entropy mode is excluded too.) Thus, on the one hand, they follow to be stable for arbitrary mean flowfields; that is, they suppress the excitation of hydrodynamic instabilities, which are a prominent problem in LEE computations. On the other hand, no vorticity exists beyond the source regions, and its dynamics is described by the source term alone in the case of the APE. This means that the source term fully controls the vorticity perturbations in an APE solution. Predicting airframe noise, this is an essential feature, since such kinds of noise are generated within the APE or LEE by the interaction of turbulent fluctuations with edges [31]. In the case of the LEE, however, vortex dynamics are partly induced by the source term but partly resolved by the governing equations too. Thus, turbulent near-field fluctuations induced by the source term in the LEE differ from the expected values, and airframe noise generation is not well controlled by the source.

As a final contribution to the discussion of Fig. 12, the channeled waves were well suited to substantiate the verification of the employed DGM based on Lagrange truncation, since they are subject to permanent refraction in the employed laminar boundary layer. However, as far as the choice of the governing equations themselves is concerned, an accurate prediction of channeled waves is actually not crucial in practical airframe noise predictions. The occurrence of airframe noise inherently means that boundary layers are turbulent and not laminar, as in the present test case. However, eddies of a turbulent boundary layer cause sound waves to be scattered, so no strong channeled waves are expected to occur. Thus, what really counts for reliable airframe noise predictions are the direct waves. As also shown in Fig. 13, the APE indeed capture them well.

Figure 13 focuses on the directivities from APE and LEE from Fig. 12. But, in contrast to that figure, Fig. 13 compares unscaled pressure rms values, i.e., $\Gamma(\theta) = \tilde{p}(\theta)$. The only difference between the underlying PIANO computations is the set of governing equations that was solved. Figure 13 clearly proves that the APE predict the direct sound field well. Converted into sound pressure levels, the peak amplitude deviates less than 1 dB.

3. *Critical Angle*

Besides performing direct numerical simulations, Suzuki and Lele also derived analytic solutions (i.e., Green's functions) for the sound field of a monopole source in a boundary layer [12,13]. They are based on the linearized Lilley's equation and were either derived in the high- or low-frequency limit for an observer in the far field. According to the high-frequency Green's function, direct waves can not propagate beyond the so-called critical angle θ_{crit}, and the peak amplitude is expected right at this angle, which is $\theta_{\mathrm{crit}} = 126.29°$ for $Ma_\infty = 0.3$ [13].

The respective peak associated to the direct waves indeed appears very close to the critical angle in the various simulations [see Fig. 12 (left)], namely, at $\theta \approx 126°$ using the APE and at $\theta \approx 129°$ in the DNS or using the LEE. The apparently perfect agreement of the peak

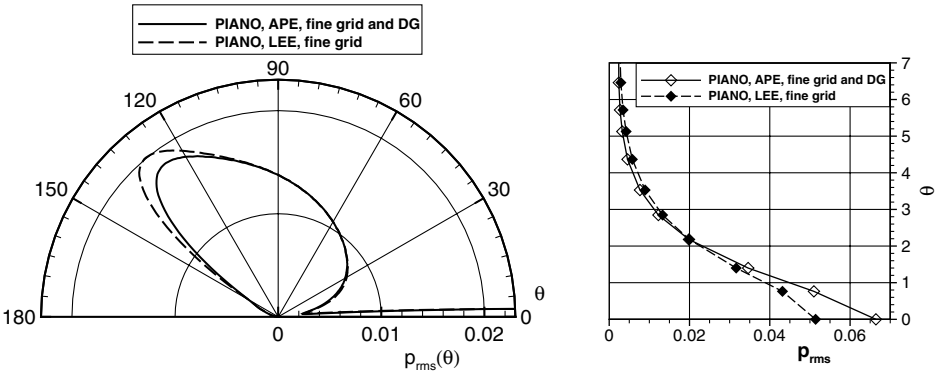

Fig. 13 Unscaled directivities $\Gamma(\theta) = \tilde{p}(\theta)$ of monopole in boundary layer from PIANO using APE on the one hand and LEE on the other hand; the right graph is a close-up of the channeled wave region.

angle from the APE with the critical angle seems somewhat fortuitous, though. As shown in [13], the directivities from DNS depend on the radius of the directivity path, which usually was $r = 15$. As the radius increased, the peak angle from DNS was found to decrease, i.e., to approach the critical angle. In turn, the peak angle from the APE is expected to fall below the critical angle. Recall that the Green's functions were derived for the far field. Furthermore, note that the high-frequency Green's function assumes an infinitesimal ratio of acoustic wavelength and boundary-layer thickness, $\lambda/\delta \to 0$, whereas $\lambda/\delta \approx 1$ in all computations.

IV. Conclusions

The proposed DGM based on Lagrange truncation was confirmed to work excellently. Computations were stable and free from any spurious numerical oscillations. Perfect agreement with PIANO-APE results is observed. The agreement with results from DNS or theory (critical angle) is good. Most of the little deviations are just due to the simplified wave operator encoded in the APE.

A ratio of triangle edge length to resolvable acoustic wavelength of $\frac{L}{\lambda} \leq \frac{1}{3}$ should be realized in a DG grid if highly accurate results are required. However, coarser grids of ratio $\frac{L}{\lambda} \leq \frac{1}{2}$ have been found to be sufficient for practical purposes [3].

Nevertheless, the proposed DG method may also be improved in some regard. First, considering the spatial DG discretization, there may be a more efficient arrangement of the Lagrangian nodes than the one suggested in Fig. 2, which makes nodes from neighboring elements coincide along element edges. It may be advantageous to arrange the nodes more homogeneously in the overall grid instead. Thus, one may be able to increase element size without loosing accuracy, resulting in fewer elements and a larger time step.

Second, time integration can probably be improved too. The employed standard Runge–Kutta scheme may be replaced by a scheme tailored to the requirements of CAA, like the low-dissipation and low-dispersion Runge–Kutta scheme of Hu et al. [32].

Appendix: Coordinate Transformation for Calculation of Surface Integrals

To calculate the surface integrals from Eq. (11), local element coordinate systems $\Sigma^{(m)}$ are introduced in addition to the global coordinate system Σ; see Fig. A1. The global Σ coordinate system (coordinates x and y) is defined by origin $\boldsymbol{O}$ and basis vectors i_x and i_y. On the other hand, the local element coordinate system $\Sigma^{(m)}$ for element $E^{(m)}$ (coordinates $\xi^{(m)}$ and $\eta^{(m)}$) is defined by origin $\boldsymbol{O}^{(m)}$ and basis vectors $\boldsymbol{i}_\xi^{(m)}$ and $\boldsymbol{i}_\eta^{(m)}$. The length of $\boldsymbol{i}_\xi^{(m)}$ and $\boldsymbol{i}_\eta^{(m)}$ is one in the $\Sigma^{(m)}$ coordinate system but generally not one in the global Σ coordinate system. The origin $\boldsymbol{O}^{(m)}$ is vertex 1 of triangle $E^{(m)}$. The relationship between the coordinates is

$$\begin{aligned} x &= x_1^{(m)} + \xi^{(m)}(x_2^{(m)} - x_1^{(m)}) + \eta^{(m)}(x_3^{(m)} - x_1^{(m)}) \\ y &= y_1^{(m)} + \xi^{(m)}(y_2^{(m)} - y_1^{(m)}) + \eta^{(m)}(y_3^{(m)} - y_1^{(m)}) \end{aligned} \tag{A1}$$

which evaluates to

$$\begin{aligned} \xi^{(m)} &= [x(y_3^{(m)} - y_1^{(m)}) + y(x_1^{(m)} - x_3^{(m)}) \\ &\quad + x_3^{(m)} y_1^{(m)} - x_1^{(m)} y_3^{(m)}]/J^{(m)} \\ \eta^{(m)} &= [x(y_1^{(m)} - y_2^{(m)}) + y(x_2^{(m)} - x_1^{(m)}) \\ &\quad + x_1^{(m)} y_2^{(m)} - x_2^{(m)} y_1^{(m)}]/J^{(m)} \end{aligned} \tag{A2}$$

where $J^{(m)}$ is the Jacobian

$$J^{(m)} = (x_2^{(m)} - x_1^{(m)})(y_3^{(m)} - y_1^{(m)}) - (x_3^{(m)} - x_1^{(m)})(y_2^{(m)} - y_1^{(m)}) \tag{A3}$$

The symbol $y_1^{(m)}$, for example, denotes the y coordinate of vertex 1 of triangle $E^{(m)}$.

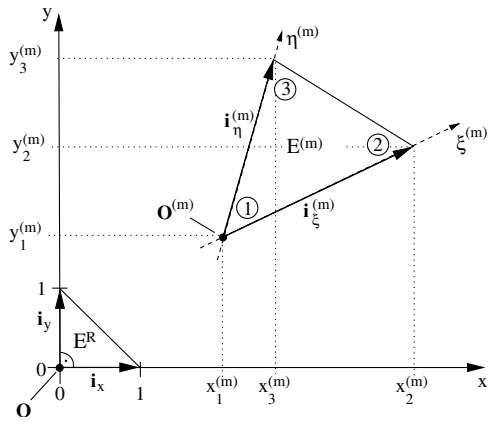

Fig. A1 Illustration of the relationship between the global Σ coordinate system with coordinates x and y, and a local $\Sigma^{(m)}$ element coordinate system with coordinates $\xi^{(m)}$ and $\eta^{(m)}$.

Acknowledgments

This work was supported by the German Federal Ministry of Economics and Technology (BMWI) under grant number 20A0603F, reference number 165 (Umströmungsgeräuschsimulation für hochkomplexe Geometrien mittels unstrukturierter Diskretisierung). The authors would like to thank T. Suzuki and S. K. Lele for providing their direct numerical simulation data from the test case of a monopole in a boundary layer.

References

[1] Ewert, R., Meinke, M., and Schröder, W., "Computation of Trailing Edge Noise via LES and Acoustic Perturbation Equations," AIAA Paper 2002-2467, 2002.

[2] Ewert, R., "Broadband Slat Noise Prediction Based on CAA and Stochastic Sound Sources from a Fast Random Particle-Mesh (RPM) Method," *Computers and Fluids*, Vol. 37, No. 4, 2008, pp. 369–387. doi:10.1016/j.compfluid.2007.02.003

[3] Bauer, M., and Ewert, R., "Slat Noise Prediction Using Discontinuous Galerkin Method and Stochastic Turbulent Sound Source," AIAA Paper 2010-3832, 2010.

[4] Ewert, R., and Schröder, W., "Acoustic Perturbation Equations Based on Flow Decomposition via Source Filtering," *Journal of Computational Physics*, Vol. 188, No. 2, 2003, pp. 365–398. doi:10.1016/S0021-9991(03)00168-2

[5] Ewert, R., Yin, J., and Delfs, J. W., "Simulation of Multigeometry Scattering Problems and the Radiation and Refraction of Acoustic Waves through a Shear Layer with Instability Waves Suppressed," *Fourth Computational Aeroacoustics (CAA) Workshop on Benchmark Problems*, NASA CP 2004-212954, 2004, pp. 241–254.

[6] Ewert, R., "RPM: The Fast Random Particle-Mesh Method to Realize Unsteady Turbulent Sound Sources and Velocity Fields for CAA Applications," AIAA Paper 2007-3506, 2007.

[7] Rasetarinera, P., Kopriva, D. A., and Hussaini, M. Y., "Discontinuous Spectral Element Solution of Aeroacoustic Problems," *Third Computational Aeroacoustics (CAA) Workshop on Benchmark Problems*, NASA CP 2000-209790, 2000, pp. 103–115.

[8] Rasetarinera, P., Kopriva, D. A., and Hussaini, M. Y., "Discontinuous Spectral Element Solution of Acoustic Radiation from Thin Airfoils," *AIAA Journal*, Vol. 39, No. 11, 2001, pp. 2070–2075. doi:10.2514/2.1229

[9] Ehrenfried, K., Meyer, C., and Dillmann, A., "Simulation of Sound Propagation in Boundary Layers Based on Möhring's Acoustic Analogy," AIAA Paper 2003-3272, 2003.

[10] Rao, P. P., and Morris, P. J., "Application of a Generalized Quadrature Free Discontinuous Galerkin Method in Aeroacoustics," AIAA Paper 2003-3120, 2003.

[11] Rao, P. P., "High Order Unstructured Grid Methods for Computational Aeroacoustics," Ph.D. Thesis, Pennsylvania State Univ., University Park, PA, 2004.

[12] Suzuki, T., and Lele, S. K., "Green's Functions in a Boundary Layer: Low and High Frequency Asymptotes," AIAA Paper 2000-2071, 2000.

[13] Suzuki, T., and Lele, S. K., "Green's Functions for a Source in a Boundary Layer: Direct Waves, Channelled Waves and Diffracted Waves," *Journal of Fluid Mechanics*, Vol. 477, 2003, pp. 129–173.

doi:10.1017/S0022112002003099
[14] Roe, P. L., "Approximate Riemann Solvers, Parameter Vectors, and Difference Schemes," *Journal of Computational Physics*, Vol. 43, No. 2, 1981, pp. 357–372. doi:10.1016/0021-9991(81)90128-5
[15] Hu, F. Q., and Atkins, H. L., "Eigensolution Analysis of the Discontinuous Galerkin Method with Nonuniform Grids: I. One Space Dimension," *Journal of Computational Physics*, Vol. 182, No. 2, 2002, pp. 516–545. doi:10.1006/jcph.2002.7184
[16] Zienkiewicz, O. C., Taylor, R. L., and Zhu, J. Z., *The Finite Element Method: Its Basis and Fundamentals*, 6th ed., Elsevier Butterworth-Heinemann, New York, 2005.
[17] Atkins, H. L., and Lockard, D. P., "A High-Order Method Using Unstructured Grids for the Aeroacoustic Analysis of Realistic Aircraft Configurations," AIAA Paper 1999-1945, 1999.
[18] Lockard, D. P., and Atkins, H. L., "Efficient Implementations of the Quadrature-Free Discontinuous Galerkin Method," AIAA Paper 1999-3309, 1999.
[19] Atkins, H. L., and Shu, C.-W., "Quadrature-Free Implementation of the Discontinuous Galerkin Method for Hyperbolic Equations," AIAA Paper 1996-1683, 1996.
[20] Atkins, H. L., and Shu, C.-W., "Quadrature-Free Implementation of Discontinuous Galerkin Method for Hyperbolic Equations," *AIAA Journal*, Vol. 36, No. 5, 1998, pp. 775–782. doi:10.2514/2.436
[21] Atkins, H. L., "Continued Development of the Discontinuous Galerkin Method for Computational Aeroacoustic Applications," AIAA Paper 1997-1581, 1997.
[22] Ehrenfried, K., "Absorbing Boundary Conditions for a Linear Hyperbolic System with Uniformly Characteristic Boundary," AIAA Paper 2004-2968, 2004.
[23] Dumbser, M., "Arbitrary High Order Schemes for the Solution of Hyperbolic Conservation Laws in Complex Domains," Ph.D. Thesis, Univ. of Stuttgart, Germany, 2005.
[24] Cowper, G. R., "Gaussian Quadrature Formulas for Triangles," *International Journal for Numerical Methods in Engineering*, Vol. 7, No. 3, 1973, pp. 405–408. doi:10.1002/nme.1620070316
[25] Press, W. H., Flannery, B. P., Teukolsky, S. A., and Vetterling, W. T., *Numerical Recipes in FORTRAN 77: The Art of Scientific Computing*, 2nd ed., Cambridge Univ. Press, New York, 1992, pp. 27–31.
[26] Delfs, J. W., Bauer, M., Ewert, R., Grogger, H. A., Lummer, M., and Lauke, T. G. W., *Numerical Simulation of Aerodynamic Noise with DLR's Aeroacoustic Code PIANO (Version 5.2) Manual*, DLR, German Aerospace Center, Braunschweig, Germany, 2008.
[27] Tam, C. K. W., and Webb, J. C., "Dispersion-Relation-Preserving Finite Difference Schemes for Computational Acoustics," *Journal of Computational Physics*, Vol. 107, No. 2, 1993, pp. 262–281. doi:10.1006/jcph.1993.1142
[28] Tam, C. K. W., and Dong, Z., "Wall Boundary Conditions for High-Order Finite-Difference Schemes in Computational Aeroacoustics," *Theoretical and Computational Fluid Dynamics*, Vol. 6, Nos. 5–6, 1994, pp. 303–322. doi:10.1007/BF00311843
[29] Tam, C. K. W., Webb, J. C., and Dong, Z., "A Study of the Short Wave Components in Computational Acoustics," *Journal of Computational Acoustics*, Vol. 1, No. 1, 1993, pp. 1–30. doi:10.1142/S0218396X93000020
[30] Thompson, K. W., "Time Dependent Boundary Conditions for Hyperbolic Systems," *Journal of Computational Physics*, Vol. 68, No. 1, 1987, pp. 1–24. doi:10.1016/0021-9991(87)90041-6
[31] Bauer, M., "Computation of Trailing Edge Noise with a Discontinuous Galerkin Method," *Notes on Numerical Fluid Mechanics and Multidisciplinary Design*, Vol. 112, Springer–Verlag, New York, 2010, pp. 489–496.
[32] Hu, F. Q., Hussaini, M. Y., and Manthey, J. L., "Low-Dissipation and Low-Dispersion Runge–Kutta Schemes for Computational Acoustics," *Journal of Computational Physics*, Vol. 124, No. 1, 1996, pp. 177–191. doi:10.1006/jcph.1996.0052

J. Astley
Associate Editor